Nanotopographic characterization of microfractures in rocks by Atomic Force Microscopy

Joanna Gurgurewicz[a,*], Daniel Mège[a,b], Marta Skiścim[c,d], Justyna Pers[d]

[a] Space Research Centre, Polish Academy of Sciences, Bartycka St. 18A, PL-00716 Warsaw, Poland
[b] Laboratoire de Planétologie et Géodynamique, UMR CNRS 6112, Université de Nantes, 2 rue de la Houssinière, 44322 Nantes, France
[c] Institute of Geological Sciences, Polish Academy of Sciences, Research Centre in Wrocław, Podwale St. 75, PL-50449 Wrocław, Poland
[d] University of Wrocław, Institute of Experimental Physics, pl. M. Borna 9, PL-50204 Wrocław, Poland

ARTICLE INFO

ABSTRACT

The study of microfractures is one of the keys to understand a variety of geological issues as diverse as seismic rupturing mechanisms, process zone characterization and evolution toward large-scale fracturing, characterization of reservoirs of geological fluids, or identification of microhabitats outside Earth. In earlier works, microcrack initiation and propagation in rocks has been observed at microscale. We test Atomic Force Microscopy (AFM) as a tool to retrieve nanoscale digital elevation models (nDTM) of rock surfaces. Basalt samples from two different geological environments are studied. In a basalt from Siberia, the topography of the granular material infilling of the crack can be accurately characterised, and the pristine crack shape retrieved, opening access to an estimate of the volume of the infilling material. In a basalt from Ethiopia, mixed-mode fracturing (opening-shear) is identified from nanofracture topography, as well as a textbook example of along-strike variations of fracture displacement. These observations demonstrate that fractures already initiate and propagate at nanoscale, and AFM is a powerful tool to conduct quantitative structural geology analyses with a resolution of ~1 nm.

1. Introduction

Atomic Force Microscopy (AFM, Binnig et al., 1986; Eaton and West, 2010) is mostly used in physics, such as tribology (e.g., Carpick and Salmeron, 1997), and biology, where molecular resolution is obtained (e.g., Murugesapillai et al., 2017). The potential of AFM for characterization of geological materials has been investigated on the one hand in the study of grain morphology, size, and porosity of fault mirrors (Siman-Tov et al., 2013) and extraterrestrial free grains and particles (Pike et al., 2011; Bentley et al., 2016), and on the other hand, in the identification and characterization of biogenic components trapped in rocks (Steele et al., 2000; Hassenkam et al., 2017). An underestimated potential benefit of AFM is the quantitative topographic information under the simple form of a x-y-z ASCII file, i.e. a nano-Digital Terrain Model (nDTM), with a routine resolution of nanometres laterally and Ångströms vertically. This potential is especially high in structural geology, where microfracture analysis is able to document mechanisms of crack nucleation (e.g., Lockner et al., 1991) and sub-critical failure mechanisms (Voigtländer et al., 2018), helpful in determining paleostress fields (e.g., Gurgurewicz and Bartz, 2011), or

understanding microseismicity associated to large faults (Stabile et al., 2012). Microcrack opening and cementation, as well as grain shape and heterogeneity, are critical to the understanding of the genesis of process zones where propagation of larger-scale fractures initiates. Microcracks in rocks are also ideal sites to look for biologic signatures on Mars (Gasda et al., 2017). A review of applications of microfracture analysis is provided by Anders et al. (2014).

Microfracture analysis has been however limited to scales larger than ~1 μm (e.g., Menéndez et al., 2001; Onishi and Shimizu, 2005; Gomez and Laubach, 2006). In this paper we show that going to the scale ~1 nm is possible using AFM, making structural geology analysis possible with the same methods as the ones used for conventional scales. For this proof of concept we use two basaltic rock samples. It is well documented that development of fractures in solid rock does basically not depend on rock composition nor fracture kinematics (e.g., Cladouhos and Marrett, 1996; Schultz et al., 2013), suggesting that their fracturing patterns should be also found in most hard rocks.

Due to the very small AFM scanning area, frequently not more than 10×10 nm^2, coupling AFM with a technique that can provide some local context is helpful. Scanning Electron Microscopy (SEM) is a

convenient technique in this respect (Russell et al., 2001).

2. Data and methods

Basalt samples the geological context and composition of which have been characterised in earlier studies were selected (Gurgurewicz et al., 2015; Mège et al., 2015). One is from the Udokan volcanic field, Siberia, and the other one from the Gode lava flow in Ogaden, Ethiopia. The mineralogical structure and composition of these basalts is similar; both are alkali basalts, Ti-rich, with a slightly higher Ti content in the Udokan samples (Gurgurewicz et al., 2015).

The microscopic surface of samples to be scanned by AFM needs to be prepared by removing roughness. In this study, we remove as much roughness as possible by polishing, because irregular rock surfaces are difficult to interpret: the recorded topography mixes positive reliefs such as from stronger mineral surfaces and stronger infilling planes, negative reliefs due to fracture voids, and artifacts. By decreasing roughness, the amount of potential artifacts related to imperfect matching between the geometry of the AFM probe tip and the geometry of the imaged surface (e.g., Gainutdinov and Arutyunov, 2001; Nye and McIntyre, 2007; Gołek et al., 2014) is minimised, and the clearest view of negative fracture topography is obtained. The roughness and complexity of mineral structure make rock surfaces particularly prone to such artifacts, as illustrated by the AFM data retrieved from the Phoenix Lander on Mars (Smith et al., 2009; Pike et al., 2011).

AFM analysis was conducted in contact mode (Supplementary Material S1). Solid rock analysis is a challenge due to the highly heterogeneous surface of minerals of different composition, size, and strength. This heterogeneity makes the richness of observations, as well as a threat for cantilever tips and a potential source of artifacts. In order to determine how rocks samples should be prepared to minimize artifacts, three surface preparation methods were implemented: breaking with a hammer, powdering, and polishing. More details are provided in Supplementary Material S2. The hammer-cut surface is planar and sharp, which is appropriate for AFM investigations, but the sharp surface is irregular and appears striated (Fig. 1a) with stepped striations densely distributed enough to remove any mineral-related signature. The striations are very similar to slickenside striations (e.g., Blenkinsop, 2002, see his Fig. 2.19) produced by various possible mechanisms during frictional movement along a fast slipping plane in rock, and may therefore be a direct effect of hammer-cutting. Similar grooves are observed on AFM images along other types of natural structural discontinuities (Thomas et al., 2014). Powder with the mobility of some grains leaves linear traces (Fig. 1b) similar to traces observed in earlier rock powder or dust studies (e.g., Pike et al., 2011). Sample polishing allows to avoid a considerable number of scanning artifacts (Fig. 1c).

Polishing itself does produce artifacts, however they are localized and usually can be easily identified (Supplementary Material S3). They include thin polishing traces and the filling of the natural cracks with diamond dust. Polishing traces have characteristic shape, thickness, and parallelism. Sample cleaning as described in Supplementary Material S2 allows to remove loose crack infillings resulting from polishing.

SEM analysis was conducted in order to provide a context for the AFM images. Locating the same features with SEM and AFM is a challenge, even though the sample surface area is only $5 \times 5\,\text{mm}^2$, considering the difference in SEM and AFM image scales. It was achieved using a pattern grid engraved on the surface of the samples as a guide to AFM tip positioning (Supplementary Material S2). Comparative SEM-AFM analyses have already been conducted in biology (Braet et al., 1996) and materials science (e.g., Lemoine et al., 1999; Chien et al., 2006; Man et al., 2015); furthermore, a device for simultaneous AFM-SEM acquisition has been designed (Park et al., 2014). In earth sciences, SEM-AFM analysis of the same part of rock has not been reported earlier, with the exception of Chatzitheodoridis et al. (2014), who could achieve this due to the specific sample context of the studied mineral.

Quantitative analysis of AFM topography can be done using various dedicated software, including freewares WSxM (Horcas et al., 2007) and Gwyddion (Nečas and Klapetek, 2012). In this work WSxM is used.

3. Results and interpretations

3.1. SEM and AFM observations

The SEM and AFM images of the Udokan basalt (sample RN02) and the Ogaden basalt (sample WS1.2) are presented on Fig. 2. Three-dimensional views of AFM topography are also shown on Fig. 3. The nDTM data are provided as Supplementary Datasets D1 and D2. The AFM images focus on two microfractured minerals, a plagioclase crystal in sample RN02, and a pyroxene crystal in sample WS1.2. Their composition as from SEM is provided as Supplementary Material S4.

The SEM image of RN02 (Fig. 2a–b) shows an L-shaped crack, ca. 50 μm in length and 3 μm in aperture. Many such microcracks are observed on this image. Due to its sharp geometry in map view, it is inferred that the cavity is an intracrystalline crack (Kranz, 1983). The SEM image suggests that this crack is deep and mainly empty; however, the AFM topography shows that a granular material partly fills the crack (Figs. 2c and 3), making it almost flat, with surface irregularities reaching a few hundred nanometres. Crack infilling is almost undetected using SEM due to its coarser resolution. Information on the composition of this infilling material can therefore not be retrieved using SEM.

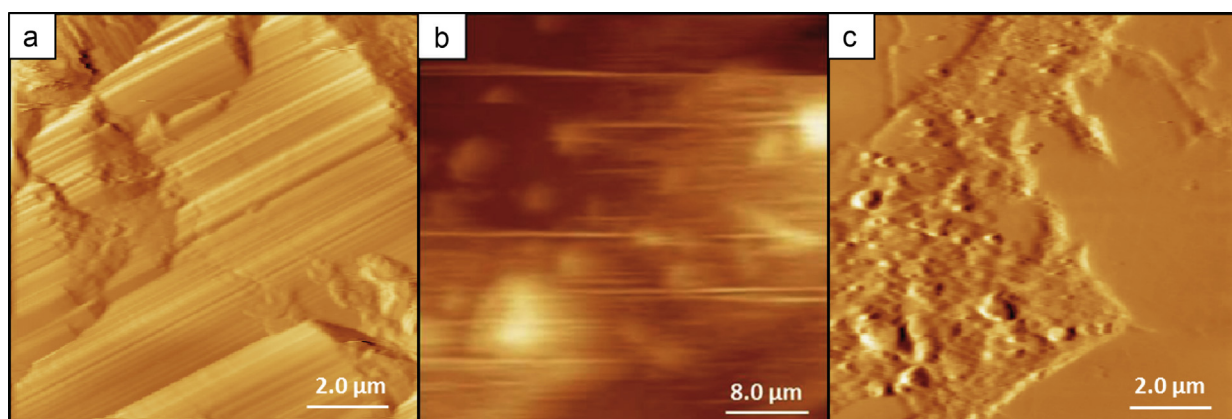In sample WS1.2, SEM reveals a deep and narrow segmented crack-

Fig. 1. AFM implementation for basalts: imaging of (a) a hammered surface, (b) a powder, (c) a polished surface. Striations in (a) are interpreted to be slickenslide striations. Artifacts in (b) are due to the mobility of grains (Gołek et al., 2014). Polishing is the only sample preparation method that provides an interpretable view of mineral topography.
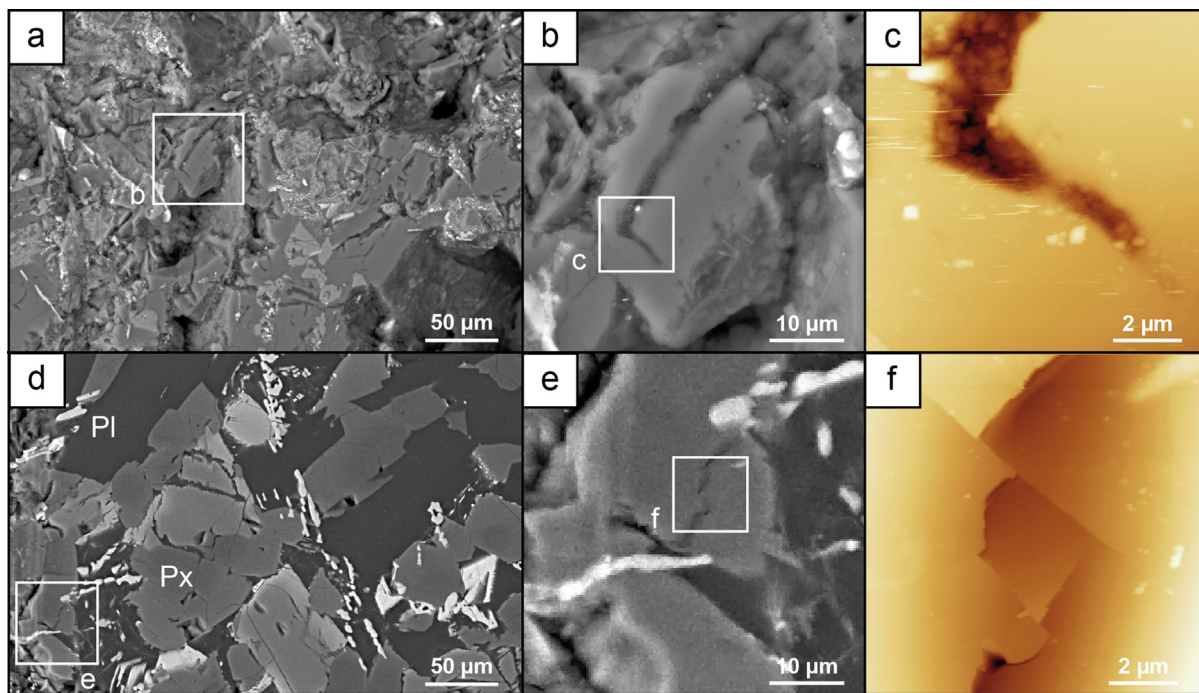
Fig. 2. SEM and AFM images of basalt samples RN02 (Udokan volcanic field, Siberia, a-c) and WS1.2 (Gode volcanics, Ogaden, Ethiopia, d-f). The AFM topography images were obtained in cracked crystals, a plagioclase (Pl) crystal in the Udokan basalt and a pyroxene (Px) crystal in the Ogaden basalt. Images (a), (b), (d), and (e) are from SEM, (c) and (f) from AFM. The AFM images have 512 × 512 data points with point spacing 19 nm.

like fracture entirely cutting a pyroxene crystal (Fig. 2d–e). Similar structures are abundant on the SEM image of WS1.2. AFM topography (Figs. 2f and 3) provides a clear view of this fracture system. The overall surface displays a two-step geometry, in which the topographic slope between the steps seems inadequately described by the word "crack" (in the sense of small-scale mode-I kinematics). The lower step (Fig. 3, on the left) is tilted toward the upper step, perhaps an effect of relative rotation. The contact between the two steps is reminiscent of gaping normal faults, in which the hanging wall is tilted, opening a shallow gap between the two faulted blocks that continues with a deeper shear fracture (e.g., Gudmundsson, 2011, ch. 9). The fracture observed on Fig. 2d–f is also associated with cross fractures visible on the AFM image only.

Faults have been reported at microscale in high-pressure

experiments (Ferrand et al., 2017) as well as nanoscale in natural rock samples (Auzende et al., 2006) within the context of crystal dehydration in the deep crust. WS1.2 was collected not far from the original surface of the lava flow. Given the geological and climatic context (Gurgurewicz et al., 2015), the fractures observed here could form in response to cyclic thermal stress (Zhou et al., 2015), with synergistic effect of solar heating and moisture (McFadden et al., 2005; Moores et al., 2008), and propagate by the growth of salt crystals in the fracture voids (Amit et al., 1993; Goudie et al., 2002) and subcritical crack growth (Voigtländer et al., 2018).
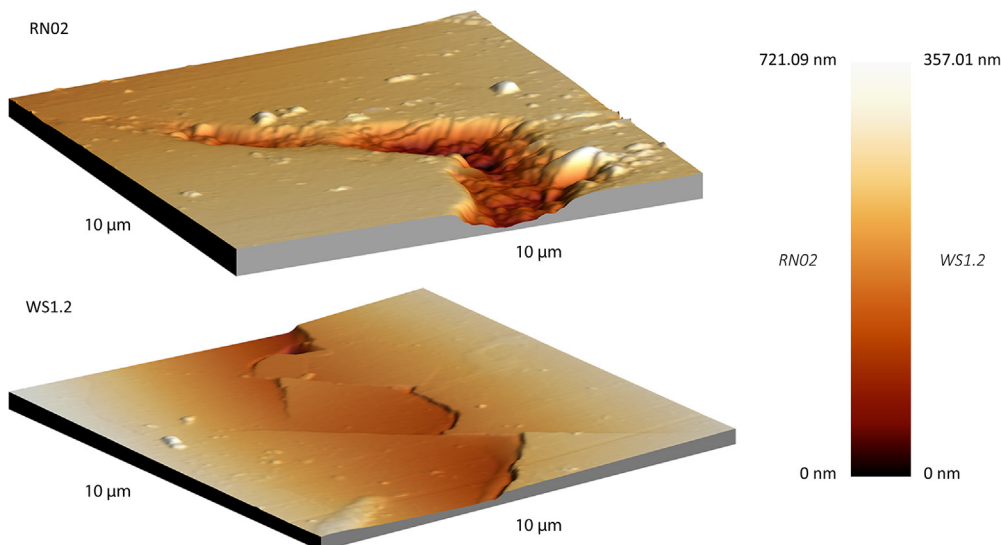

Fig. 3. Three-dimensional topographic views of samples RN02 and WS1.2.

Fig. 4. Topographic profiles of the surface of sample RN02. Upper left: Shaded relief AFM image with location of Profile A; upper right: unshaded nDTM with superimposed contours every 20 nm and location of profiles B to F. Profile A shows the corrected topographic measurement of the surface of the sample in an area devoid of structural features used to estimate the error on topographic flatness. On profile A, Z = 0 corresponds to average profile elevation. The other profiles are aligned on top, which is given the value Z = 0.

Contour spacing: 5 nm
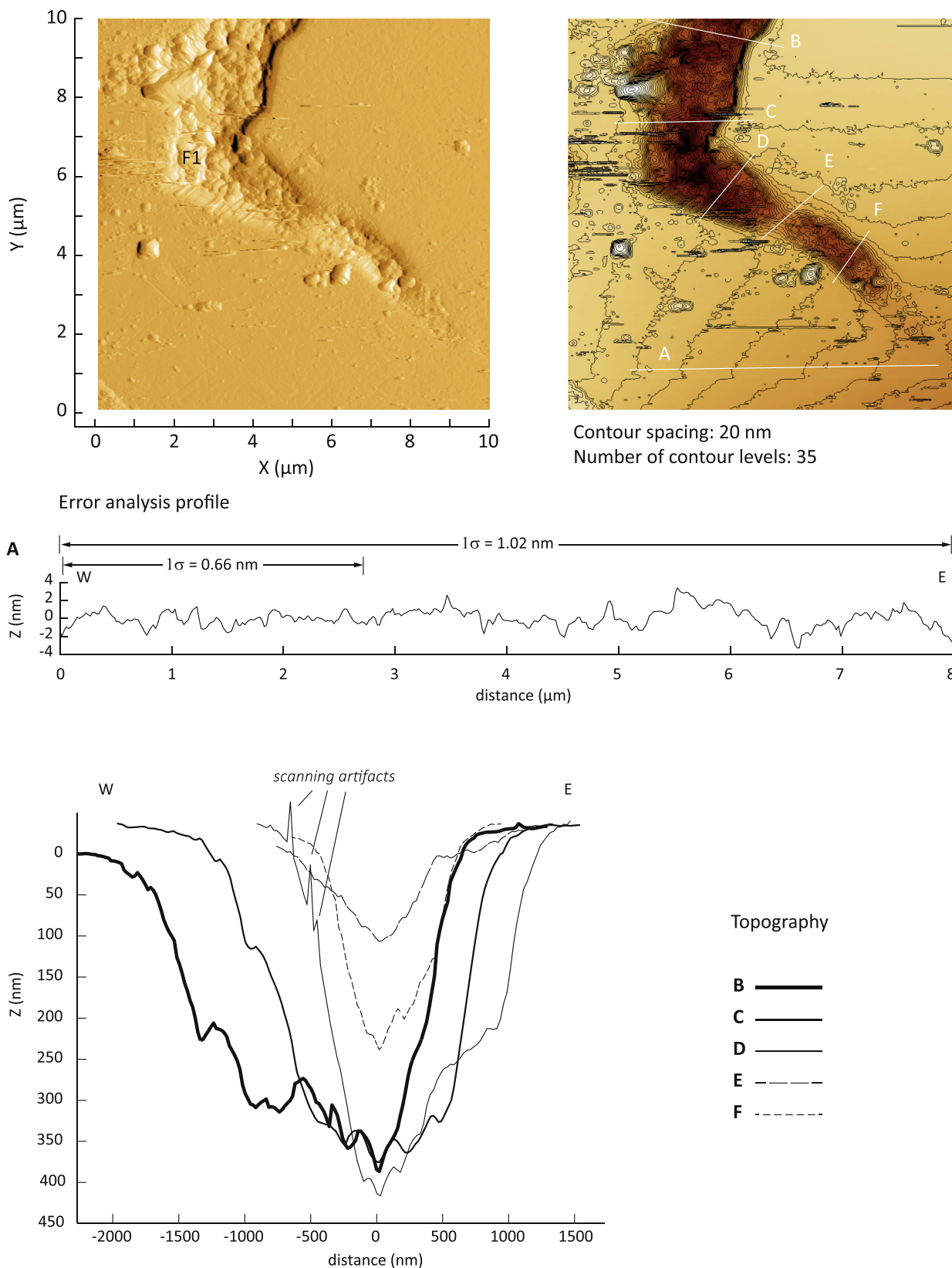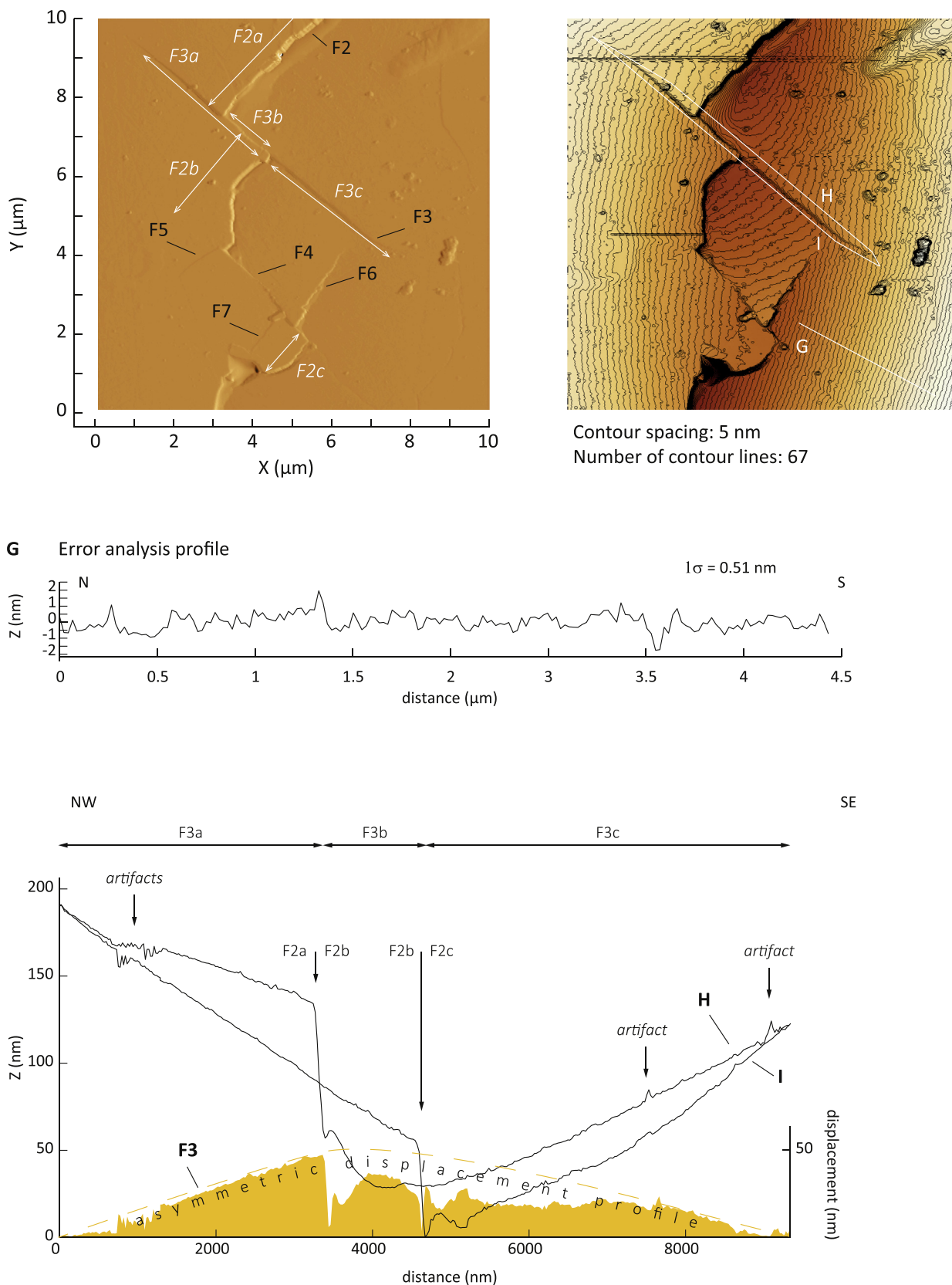Number of contour lines: 67

Fig. 5. Topographic profiles of the surface of sample WS1.2. Upper left: Shaded relief AFM image with location of Profile A; upper right: unshaded nDTM with superimposed contours every 5 nm. Profile A shows the corrected topographic measurement of the surface of the sample in an area devoid of structural features used to estimate the error on topographic flatness, which results from polishing artifacts and AFM noise. Profiles B to C are taken at the top and bottom of a cross fracture. The orange surface is fracture displacement calculated as the difference between elevations on profiles B and C. (For interpretation of the references to colour in this figure legend, the reader is referred to the Web version of this article.)

3.2. Interpretations

3.2.1. nDTM vertical error

Vertical precision error of the nDTMs is evaluated in order to determine the reliability of AFM nDTM vertical measurements. The calculation of this error is designed to empirically account for all the signal that is not related to mineral features at the polished surface of the sample. This includes electronic and mechanical noise inherent to the method, surface bumps due to nano-variations of mineral strength and nanofracture strength, and imperfect polishing. Error is estimated as the standard deviation of topography along nDTM profiles.

A profile is first identified on the basis of best possible flatness on the raw nDTM (profiles A on Fig. 4 and G on Fig. 5). Deviations from perfect flatness only result from surface slope, AFM noise as well as polishing artifacts. For sample RN02 (Fig. 4), the raw nDTM profile is corrected from surface slope by removing topographic undulations with the best polynomial fit, which here has degree 5, and detrending the resulting profile by a constant linear slope. The standard deviation along the resulting profile is $1\sigma = 0.85$ nm. For sample WS1.2 (Fig. 5), correction of the selected raw nDTM to obtain the flattest possible profile requires removing a constant slope only. The standard deviation along the profile is $1\sigma = 0.51$ nm. Details are in Supplementary Material S5.

3.2.2. Sample RN02

As an example of nDTM use for fracture analysis, topographic profiles of the surface of sample RN02 are analysed on Fig. 3. The topography of the granular material infilling of the L-shaped crack (Fig. 4, F1) can be accurately characterised and makes topographic variations tens of nanometres high at the bottom of the crack (Fig. 6, violet lines). Crack profiles have similar slopes in their upper part (black lines) that probably reflect the geometry of the crack before infilling. By interpolating these slopes, an idea of the pristine crack shape may be retrieved (beige lines), opening access to an estimate of the volume of the infilling material.

3.2.3. Sample WS1.2

The fracture system observed on sample WS1.2 has complex geometry and kinematics. The main fracture (Fig. 5, F2) is segmented into 3 segments (F2a-c). The segments are separated by two transverse fractures (F3, F4). F3 is also segmented into 3 parts. The middle segment (F3b) dips toward F2a and the two others dip toward F2b. F4 is a scissors shear along which the footwall of one side becomes the hanging wall of the other side. F4 ends with a wing fracture (F5) on one side, and with F2c on the other side. F4 is also connected to the largest opening of another wing fracture (F6), and to another fracture (F7). The main fracture (F2) and the transverse fractures (F3, F4) probably developed simultaneously because these relationships show that the development of F3 and F4 affected the development of F2 but F2 influenced the development of the segments of F3.

We use the nDTM of sample WS1.2 to investigate further the structure of F2 and F3. Analysis of topographic profiles taken perpendicular to F2 (Fig. 7) suggests that F2 is a mixed-mode fracture, either I–II or I–III (uncertainty arises from the absence of both fracture ends on the sample). The hanging wall of segment F2a is offset from the footwall by 115–140 nm (profiles J-M), a value that gradually decreases on F2b to ca. 70 nm (profiles O-R). An asymmetric topographic bump is observed at the top of the hanging wall, with the steeper scarp on the footwall side. The bump is unlikely to be due to some polishing effect because it is seen to be locally almost continuous with the footwall in the area of the sample around Profile M. The steeper scarp and the base of the footwall form a "moat". The topography of the hanging wall further from the footwall is usually sloping backward, toward the footwall. These topographic features are readily explained within the framework of a mixed-mode fracture. The moat accounts for mode I displacement. The bump is interpreted as a feature that accommodates mode I at the surface and shear mode at depth (e.g., Gudmundsson, 2011, see also Fig. 3 of Acocella et al., 2003). The main, 70–140 nm high scarp between the two walls, is then a consequence of this shear.

A correlation is observed between the bump and moat geometry and the topography of the hanging wall away from the footwall. The bump and the moat are best observed on profiles J and K on Fig. 7, and much poorly defined on profiles M and N, which implies higher shear at J and K. L has an intermediate geometry. The backward-tilted topography of the hanging wall is also more pronounced at J and K that M and N. Pure mode I does not generate hanging wall rotation, whereas shearing triggers rotation along the inclined shear plane. Profiles M and N show a mixed mode I plus starting shear mode, corresponding to the inset on Fig. 7 (taken from Gudmundsson, 2011) with no rotation to limited hanging wall rotation. In contrast, J and K are at a most advanced stage of shearing and displacement, where hanging wall rotation has become significant (arrow on Fig. 7 upper profile graph), a stage which is hardly found in natural landscapes due to erosion.

Similar analysis can be done with profiles O to R. The amplitude of the bump is positively correlated with backward rotation, with maximum amplitude and rotation on profile O and minimum on R. Profiles O-R, measured perpendicular to the main scarp of F2b, provide information on F2 kinematics. At the scale of the whole hanging wall crystal block, rotation is obvious on the nDTM and is spectacularly emphasized by the scissors kinematics of F4 (best viewed on Fig. 7). However, the rotation gradient is oblique to the F2b fracture segment, as illustrated by the long arrow at the surface of the rotated block on Fig. 7. Profiles that would cut F2b at the same place as profiles O-R but running parallel to the rotation gradient would give similar results, although emphasizing the topographic expression of the mixed-mode displacement on all the profiles.

On sample WS1.2, analysis of the geometry of the moat, the bump, and the remaining of the hanging wall, reveals a textbook example of along-strike variations of fracture displacement.

F3 is also useful to illustrate another aspect of fracture displacement (Fig. 5), made possible because its two lateral ends are visible on the nDTM. Fault displacement is measured as the difference in nDTM elevation between the top of the fracture (topographic profile H) and its bottom (profile I). Theoretical fracture profiles are elliptic (e.g., Walsh and Watterson, 1989), but fracture segmentation (Willemse, 1997) as well as fracture growth itself (Cartwright et al., 1995; Mansfield and Cartwright, 2001) alter this ideal displacement distribution. The effect of fracture segmentation is seen on the F3 displacement profile on Fig. 5 (orange surface), where F2 cuts F3 twice, dividing it into the three segments F3a-c. Simultaneous growth of F2 and F3 may have also affected the displacement profile of F3 by generating the observed profile asymmetry. On F2, the vertical offset of F2a is larger than that of F2b, which reflects in the larger displacement along F3a than along F3b and F3c, resulting in the overall asymmetric displacement profile.

4. Discussion

4.1. AFM and other methods

The precision of AFM topography combined with the context provided by SEM is powerful to characterize rock surfaces at nanoscale. Due to the difference in resolution, however, locating specific features on SEM and AFM is not trivial. We have proposed a procedure that allows to do this efficiently.

We show that structures on the surface of minerals may be incorrectly interpreted when SEM is used alone. In addition to composition information, SEM is able to provide topographic information, both in secondary electron and backscattered electron modes. However, in contrary to AFM, topography is not a direct and primary product of SEM, and when used for topography, SEM is usually used for visualisation only. Quantitative topography extraction method have been developed, however, based on various methods such as
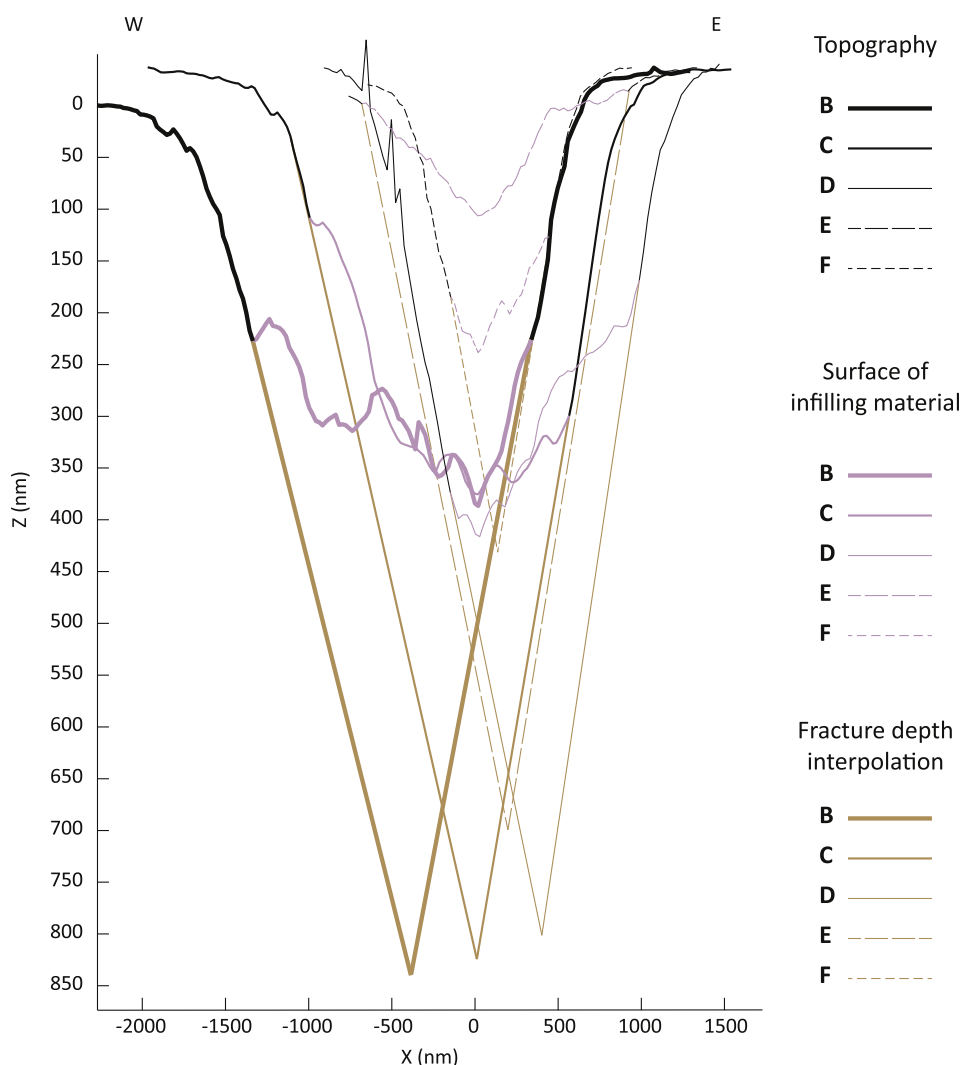
Fig. 6. Interpolation of infilled crack profiles on RN02 to retrieve an estimate of true fracture depth, assuming that the crack walls have constant structural slope. The pyroxene surface and the interpreted observed crack surface are in black, the interpreted infilling surface in violet, and the interpolated crack wall in beige. (For interpretation of the references to colour in this figure legend, the reader is referred to the Web version of this article.)

photogrammetry (e.g., Gontard et al., 2016), shape-from-shading (Butterfield et al., 2017), and multiscale image reconstruction (Tahmasebi et al., 2015). Although useful when AFM technology is not available, these methods are indirect and fail to attain the topographic detail that can be revealed by AFM directly with the cantilever tip. Moreover, conversion of SEM data to pixels does not guarantee that the pixel values reflect topography.

Furthermore, these 3D retrieval techniques also require constraining conditions of dataset acquisition which may not be obtained easily. Such difficulties are ultimately anticipated in planetary exploration, which additionally faces the problem of designing space instrumentation in which vacuum is to be made, like SEM equipment, at a reasonable cost. On the contrary, AFM technology has already been successfully implemented in space. Based on accuracy, reliability and implementation possibilities, topographic analysis of microfractures using AFM is in many cases to be favoured instead than SEM.

While SEM can provide the mineralogical context of AFM images, other methods are expected to enhance the scientific return of AFM nDTM datasets. High-angle annular dark field scanning transmission electron microscopy (ADF-STEM) may help extend AFM topography information of nanofractures to the corresponding atomic structure and originating defects (e.g., Hong et al., 2015). Cathodoluminescence may add information on internal mineral structures that potentially affect

the mineral mechanical properties and the development of microcracks, at a scale similar to AFM when the detector is mounted on a scanning transmission electronic microscope (Zagonel et al., 2011). Coupling AFM with infrared spectroscopy (AFM-IR) provides other option to analyse microfracture topography quantitatively while investigating composition at nanoscale with increasing sensitivity (e.g., Dazzi and Prater, 2017).

4.2. Contribution of AFM imaging to structural geology

AFM gives a detailed topographic description of mineral surfaces. Structures 10s–100s of nm in width, such as fractures or fractures infillings that may remain undetected or poorly detected otherwise, can be characterised with a vertical precision of the order of 1 nm. The exposed surface of granular material in fractures can be studied, which makes possible reasonable inferences on grain volumes (Fig. 4) and even crack depth (Fig. 6), and nanofracture displacements can quantified with a precision that makes possible analysis of fracture displacement and interactions (Fig. 5) as well as kinematics (Fig. 7).

It is remarkable and promising for future AFM-based nanostructural geology that structural analysis can be conducted on a polished mineral surface. Figs. 5 and 7 especially illustrate that polishing conducted as in this work does not result in a perfectly flat surface that would remove
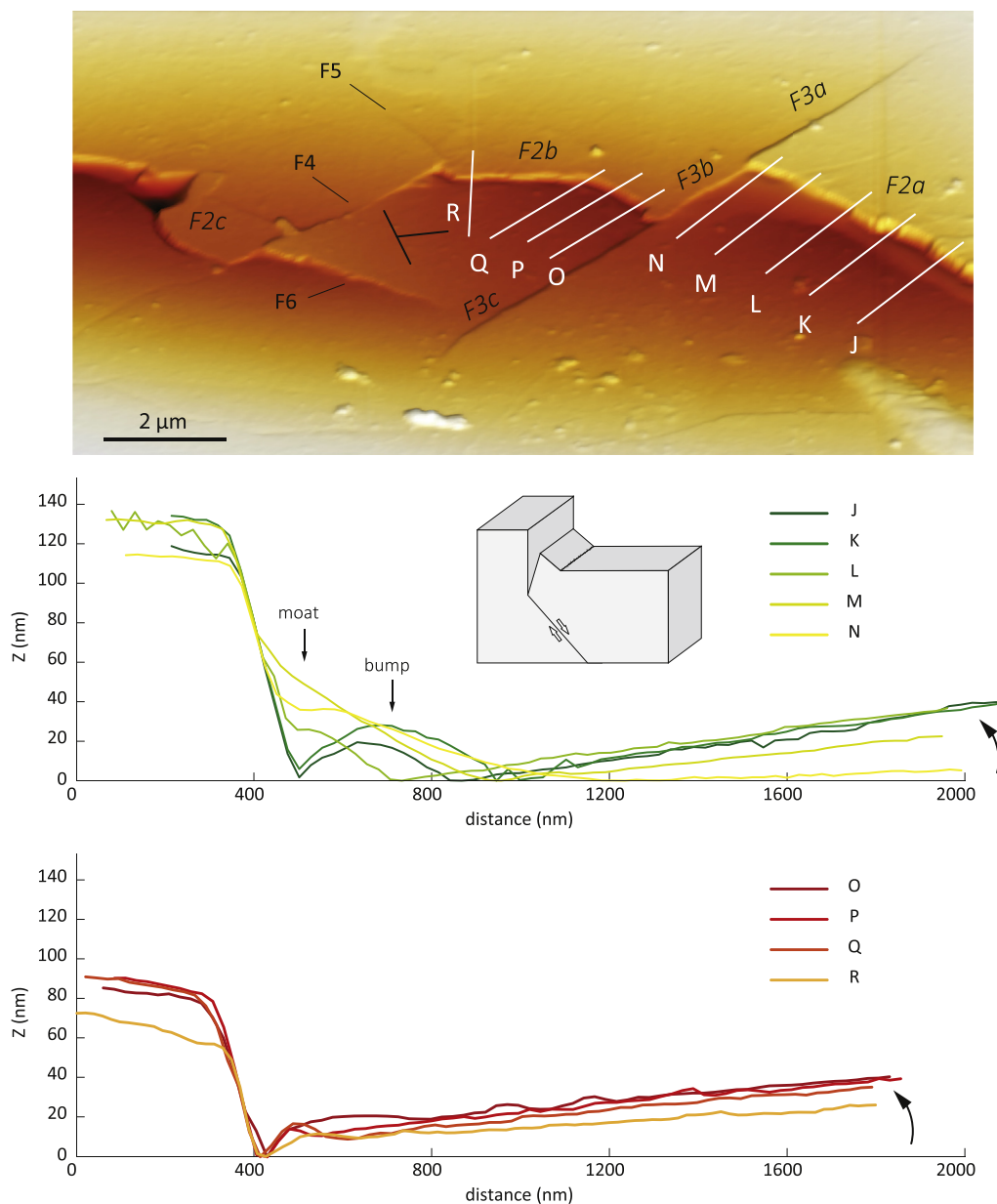
Fig. 7. AFM topographic profiles across the main fracture (F2) of sample WS1.2. The nDTM suggests that the fracture is mixed mode shear. The curved arrows on the graphs indicate the interpreted sense of rotation of the hanging wall with increasing fracture displacement. The dip symbol on the oblique view underlines the sense of pyroxene crystal block rotation. The inset is from Gudmundsson (2011).

most of the structural information carried by the observed mineral. Polishing preserves some useful topographic features of structural origin, and might even highlight them by favouring topographic moulding of resistant mineral surfaces. Then, interpretations that can be done are, from this point of view, similar to the interpretations that can be done by structural analysis of landforms in the field, with polishing removing not more than erosional agents do at macroscale, with easier abrasion of weak than strong material. Further studies on other samples, especially with more control on the angle between the polished surface and planar structures such as crystal lattices, cleavage planes, or grain boundaries, may help confirm this observation and provide constraints so that preservation of this structural topography is maximised.

We show that nanotopographic depressions are windows to the geometry of the true bottom of microcracks and grain size boundaries in infillings, which can be used for e.g. fractographic analysis and characterising fluid circulation and secondary crystallisation processes.

The choice of the cantilever tip is however critical because depending on the crack shape relative to the steepness of the AFM cantilever tip, the shape of the bottom of the crack may be incorrectly imaged due to tip interference (Gainutdinov and Arutyunov, 2001; Gołek et al., 2014).

5. Perspectives

5.1. Fracture nucleation and propagation

We showed that topographic analysis of microfractures on AFM nDTM can be conducted quantitatively similar to topographic analysis of macroscopic fractures, especially for displacement, but also kinematics, and found that even at nanoscale, analysis can be conducted as it would be done at macroscale.

The modern notion of fractures is based on simplified analysis (Irwin, 1958) of elliptic cracks at microscopic scale (Inglis, 1913; Griffith, 1921; Westergaard, 1939) that start to grow following damage
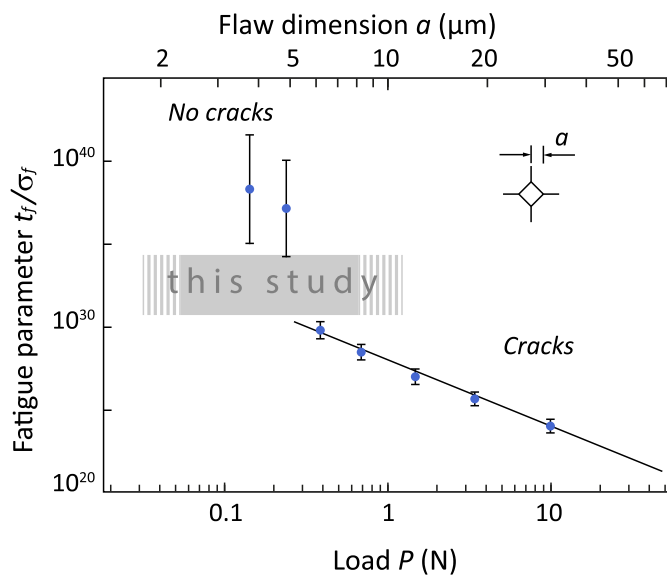
Fig. 8. The transition between flaws and propagating cracks, compared to the scale of structures studied in this work (for which the vertical scale does not apply). The data points are for increasing indentation loads from left to right by a pyramidal indenter of radius a. P is peak load. The fatigue parameter (t_f is lifetime and σ_f is failure stress) allows to identify the threshold between conditions of crack initiation from flaws (upper left data points) and crack propagation (lower left). Figure modified from Lawn (1983).

at the crack tip (Sneddon, 1946) where stress concentrates. Lawn (1983) modelled propagation from a sharp crack tip surrounded by a process zone, which he defined as a "concentrated, highly stressed volume within which discrete 'energy sinks' are activated". He showed that the key to the understanding of crack propagation lies in observing processes at atomic scale, which is relevant to AFM investigations. He also insisted that the 'submicroscopic flaws' from which microcracks grow are by default treated as equivalent to microcracks, although there is no evidence for this. Experimental data indeed argue that below some flaw size, flaw failure does not result in microcrack *propagation*, but rather *initiation*. This dimension, below which flaws are not well characterised, was proposed to be on the order of a micron, from indentor experiments (Lawn, 1983). The observations we are reporting suggest that at the scale of a micron, not only cracks, but also shears, can develop. Fig. 8 shows that the scale of the structures discussed in this paper corresponds to the scale were microfractures are just at the initiation-propagation transition. The precision of possible measurements, on the order of 1 nm, suggests that fractures that are even smaller can be accurately studied, as well as their displacement. AFM is the appropriate tool to study the transition from unpropagated flaws such as defects at atomic scale, which can be identified in parallel with ADF-STEM (Hong et al., 2015) to pristine microcracks and their well-known properties that found the current understanding of fundamental structural geology mechanisms (e.g., Atkinson, 1987), such as process zone development. Process zone size in granular rock samples is typically 5 mm (Friedman et al., 1972; in the field process zones can however be much larger, see e.g., Delaney et al., 1986; Gudmundsson, 2011), confirming that a developing process zone starts at AFM scale before its study can be undertaken using more conventional structural geology equipment and methods (Schultz et al., 2013; Soyan and Gloaguen, 2011). In a given material, process zone nature and growth may be investigated by determining the relative role of microcracking and other processes that may influence unlinear crack propagation in process zone leading to macroscale fracturing, such as transformations (Evans, 1988) at submineral scale (metamorphic, twinning) and gliding at mineral boundaries (Voigtländer et al., 2018), with implications for the deformability of rock masses (e.g., Schultz, 1995) and seismology

(e.g., Reches and Lockner, 2010). AFM may be also used as a technique to identify nanoscopic criteria for refining paleostress magnitude determination from analysis of twinning planes (Jamison and Spang, 1976; Rowe and Rutter, 1990), which is subject to large uncertainty (Lacombe, 2001).

5.2. Landscape development

In other circumstances, microcrack growth does not lead to macroscopic failure, instead it is a fundamental mechanism of gradual surface rock fragmentation. This is the case with sample WS1.2, collected at the surface of a 400 + km long lava flow exposed to erosion since 7.46 ± 0.5 Ma (Mège et al., 2015). The outcrop surface is a cobble and pebble field (Gurgurewicz et al., 2015), where rock fragmentation results from chemical alteration of basaltic joints and microcracks in response to temperature cycles, water, abundance and composition of dissolved salts, ice, and other parameters (e.g., Goudie et al., 2002; Moores et al., 2008). Nucleation and growth of microfractures as seen by AFM may therefore shed light into fundamental processes of landscape evolution.

5.3. Planetary sciences and exobiology

AFM has been successfully implemented in exploration of the Solar System, including Mars (FAMARS onboard the Mars Phoenix lander, Pike et al., 2011) and comet Churyumov-Gerasimenko (MIDAS onboard the Rosetta spacecraft, Bentley et al., 2016). FAMARS was investigating the Martian soil, and MIDAS cometary dust. This work suggests directions for the design of adapted polishing tools for planetary science applications on solid rock. Microcracks are to be a priority target for the search for biosignatures on Mars: ultraviolet radiations dissociate organic molecules in the Martian surface environment (Moores and Schuerger, 2012); microcracks in rocks may shelter microorganisms from dissociation and as a consequence should provide adequate habitats for their development, as demonstrated in polar regions on Earth (Cockell et al., 2003). AFM is already a key technology for the search of biosignatures in ancient rocks; Hassenkam et al. (2017) used it to characterize the earliest evidence of life on Earth, whereas Steele et al. (2000) used it to close a debate about the origin of biological nanostructures in Martian meteorite ALH84001. AFM is therefore able to characterize quantitatively microcracks in Martian rocks as well as potential biosignatures without the risk of terrestrial contamination.

5.4. Other perspectives

In radiochronologic dating, such as by $^{40}Ar/^{39}Ar$, AFM could make possible to examine early stages of sericitisation, which was shown to significantly alters age quality even for a minuscule amount of sericite (Verati and Jourdan, 2013). A huge field of applications arises from the possibility of using AFM nanotopography data quantitatively, as the primary output of AFM analysis is a nanoscale digital terrain model (nDTM) in ASCII format. Using the methodology presented here, generation of a nDTM which is statistically representative of a rock sample can be obtained by mosaicking adjacent AFM topographic scans. Performing series of orthogonal scans would reveal three-dimensional quantification on nanofracture networks, for which applications in many fields can be expected beyond the fracture nucleation and propagation perspectives mentioned earlier, starting with reservoir fracturing (e.g., Huang et al., 2014), hydrogeological network connectivity (e.g. (Darcel et al., 2003)), and permeability generated to radiation damage (Seydoux-Guillaume et al., 2009; 2012).

Acknowledgements

by the European Union within the framework of the European Regional Development Fund. Two anonymous reviews helped clarify aspects and sharpen the focus of the manuscript.

Appendix A. Supplementary data

Supplementary data to this article can be found online at https://doi.org/10.1016/j.jsg.2019.04.010.

References

Acocella, V., Korme, T., Salvini, F., 2003. Formation of normal faults along the axial zone of the Ethiopian rift. J. Struct. Geol. 25, 503–513.

Amit, R., Gerson, R., Yaalon, D.H., 1993. Stages and rate of the gravels shattering process by salts in desert reg soils. Geoderma 57, 95–324.

Anders, M.H., Laubach, S.E., Scholz, C.H., 2014. Microfractures: a review. J. Struct. Geol. 69, 377–394.

Atkinson, B.K., 1987. Introduction to fracture mechanics and its geophysical applications. In: Arkinson, B.K. (Ed.), Fracture Mechanics of Rocks. Academic Press, pp. 1–26.

Auzende, A.-L., Guillot, S., Devouard, B., Baronnet, A., 2006. Serpentinites in an Alpine convergent setting: effects of metamorphic grade and deformation on microstructures. Eur. J. Mineral. 18, 21–33. https://doi.org/10.1127/0935-1221/2006/0018-0021.

Bentley, M.S., Schmied, R., Mannel, T., Torkar, K., Jeszenszky, H., Romstedt, J., Levasseur-Regourd, A.-C., Weber, I., Jessberger, E.K., Ehrenfreund, P., Koeberl, C., Haves, O., 2016. Aggregate dust particles at comet 67P/Churyumov-Gerasimenko. Nature 537, 73–75.

Binnig, G., Quate, C.F., Gerber, C., 1986. Atomic force microscope. Phys. Rev. Lett. 56, 930–933.

Blenkinsop, T., 2002. Deformation Microstructures and Mechanisms in Minerals and Rocks. Kluwer Academic Publishers, New York 150 p.

Braet, F., Kalle, W.H.J., De Zanger, R.B., De Grooth, B.G., Raap, A.K., Tanke, H.J., Wisse, E., 1996. Comparative atomic force and scanning electron microscopy: an investigation on fenestrated endothelial cells *in vitro*. J. Microsc. 181, 10–17.

Butterfield, N., Rowe, P.M., Stewart, E., Roesel, D., Neshyba, S., 2017. Quantitative three-dimensional ice roughness from scanning electron microscopy. J. Geophys. Res.: Atmospheres. https://doi.org/10.1002/2016JD026094.

Carpick, R.W., Salmeron, M., 1997. Scratching the surface: fundamental investigations of tribology with atomic force microscopy. Chem. Rev. 97, 1163–1194.

Cartwright, J.A., Trudgill, B.D., Mansfield, C.S., 1995. Fault growth by segment linkage: an explanation for scatter in maximum displacement and trace length data from the Canyonlands Grabens of SE Utah. J. Struct. Geol. 17, 1319–1326.

Chatzitheodoridis, A., Haigh, S., Lyon, I., 2014. A conspicuous clay ovoid in Nakhla: evidence for subsurface hydrothermal alteration on Mars with implications for astrobiology. Astrobiology 14, 651–693.

Chien, Y.-C., Mucci, A., Paquette, J., Sears, S.K., Vali, H., 2006. Comparative study of nanoscale surface structures of calcite microcrystals using FE-SEM, AFM, and TEM. Microsc. Microanal. 12, 1–9. https://doi.org/10.1017/S1431927606060247.

Cladouhos, T.T., Marrett, R., 1996. Are fault growth and linkage models consistent with power-law distributions of fault lengths? J. Struct. Geol. 18, 281–293.

Cockell, C., Rettberg, P., Horneck, G., Scherer, K., Stokes, M.D., 2003. Measurements of microbial protection from ultraviolet radiation in polar terrestrial microhabitats. Polar Biol. 26, 62–69.

Darcel, C., Bour, O., Davy, P., de Dreuzy, J.R., 2003. Connectivity properties of two-dimensional fracture networks with stochastic fractal correlation. Water Resour. Res. 39, 1272. https://doi.org/10.1029/2002WR001628.

Dazzi, A., Prater, C.B., 2017. AFM-IR: technology and applications in nanoscale infrared spectroscopy and chemical imaging. Chem. Rev. 117 (7), 5146–5173. https://doi.org/10.1021/acs.chemrev.6b00448.

Delaney, P.T., Pollard, D.D., Ziony, J.I., McKee, E.H., 1986. Field relations between dikes and joints: emplacement processes and paleostress analysis. J. Geophys. Res. 91, 4920–4938.

Eaton, P., West, P., 2010. Atomic Force Microscopy. Oxford University Press, New York 248 p.

Evans, A.G., 1988. High toughness ceramics. Mater. Sci. Eng. A105/106, 65–75.

Ferrand, T.P., Hilairet, N., Incel, S., Deldicque, D., Labrousse, L., Gasc, J., Renner, J., Wang, Y., Green, H.W., II, Schubnel, A., 2017. Dehydration-driven stress transfer triggers intermediate-depth earthquakes. Nat. Commun. 8, 15247. https://doi.org/10.1038/ncomms15247.

Gainutdinov, R.V., Arutyunov, P.A., 2001. Artifacts in Atomic Force Microscopy: Russian Microelectronics, vol. 30. pp. 219–224.

Gasda, P.J., Haldeman, E.B., Wiens, R.C., Rapin, W., Bristow, T.F., Bridges, J.C., Schwenzer, S.P., Clark, B., Herkenhoff, K., Frydenvang, J., Lanza, N.L., Maurice, S., Clegg, S., Delapp, D.M., Sanford, V.L., Bodine, M.R., McInroy, D., 2017. In situ detection of boron by ChemCham on Mars. Geophys. Res. Lett. 44, 8739–8748.

Gomez, L.A., Laubach, S.E., 2006. Rapid digital quantification of microfracture populations. J. Struct. Geol. 28, 408–420.

Gontard, L., Schierholz, R., Yu, S., Cintas, J., Dunin-Borkowski, R.E., 2016. Photogrammetry of the three-dimensional shape and texture of a nanoscale particle using scanning electron microscopy and free software. Ultramicroscopy 169, 80–88.

Goudie, A.S., Wright, E., Viles, H.A., 2002. The roles of salt (sodium nitrate) and fog in weathering: a laboratory simulation of conditions in the northern Atacama Desert, Chile. Catena 48, 255–266.

Gołek, F., Mazur, P., Ryszka, Z., Zuber, S., 2014. AFM image artifacts. Appl. Surf. Sci. 304, 11–19.

Griffith, A.A., 1921. The phenomena of rupture and flow in solids. Philos. Trans. R. Soc. Lond. Ser. A Contain. Pap. Math. Phys. Char. 221, 163–198. https://doi.org/10.1098/rsta.1921.0006.

Gudmundsson, A., 2011. Rock Fractures in Geological Processes. Cambridge Univ. Press 578 p.

Gurgurewicz, J., Bartz, W., 2011. Deformational history of metavolcanic rocks from the Kamieniec Ząbkowicki Metamorphic Belt (Fore-Sudetic Block, southwest Poland): a quartz [c]-axis lattice preferred orientation study. Acta Geol. Pol. 61, 289–305.

Gurgurewicz, J., Mège, D., Carrère, V., Gaudin, A., Kostylew, J., Morizet, Y., Purcell, P.G., Le Deit, L., 2015. Inferring alteration conditions on Mars: insights from near-infrared spectra of terrestrial basalts altered in cold and hot arid environments. Planet. Space Sci. 119, 137–154.

Hassenkam, T., Anderson, M.P., Dalby, K.N., Mackenzie, D.M.A., Rosing, M.T., 2017. Elements of Eoarchean life trapped in mineral inclusions. Nature 548, 78–81.

Hong, J., Hu, Z., Probert, M., Li, K., Lv, D., Yang, X., Gu, L., Mao, N., Feng, Q., Xie, L., Zhang, J., Wu, D., Zhang, Z., Jin, C., Ji, W., Zhang, X., Yuan, J., Zhang, Z., 2015. Exploring atomic defects in molybdenum disulphide monolayers. Nat. Commun. 6, 6293. https://doi.org/10.1038/ncomms7293.

Horcas, I., Fernández, R., Gómez-Rodríguez, J.M., Colchero, J., Gómez-Herrero, J., Baro, A.M., 2007. WSXM: a software for scanning probe microscopy and a tool for nanotechnology. Rev. Sci. Instrum. 78, 013705.

Huang, J., Safari, R., Mutlu, U., Burns, K., Geldmacher, I., 2014. Natural-hydraulic fracture interaction: microseismic observations and geomechanical predictions. Interpretation 3, SU17–SU31. https://doi.org/10.1190/INT-2014-0233.1.

Inglis, C.E., 1913. Stresses in a plate due to the presence of cracks and sharp corners. Trans. Inst. Naval Archit. 55, 219–241.

Irwin, G.R., 1958. Fracture. In: Flügge, S. (Ed.), Encyclopedia of Physics, VI, Elasticity and Plasticity, pp. 551–590.

Jamison, W.R., Spang, J.H., 1976. Use of calcite twin lamellae to infer differential stress. Geol. Soc. Am. Bull. 87, 868–872.

Kranz, R.L., 1983. Microcracks in rocks: a review. Tectonophysics 100, 449–480.

Lacombe, O., 2001. Paleostress magnitudes associated with development of mountain belts: insights from tectonic analysis of calcite twins in the Taiwan foothills. Tectonics 20, 834–849.

Lawn, B.R., 1983. Physics of fracture. J. Am. Ceram. Soc. 66, 83–91.

Lemoine, P., Lamberton, R.W., Ogwu, A.A., Zhao, J.F., Maguire, P., McLaughlin, J., 1999. Complementary analysis techniques for the morphological study of ultrathin amorphous carbon films. J. Appl. Phys. 86, 6564. https://doi.org/10.1063/1.371615.

Lockner, D.A., Byerlee, J.D., Kuksenko, V., Ponomarev, A., Sidorin, A., 1991. Quasi-static growth and shear fracture energy in granite. Nature 350, 39–42.

Man, J., Valtr, M., Petrenec, M., Dluhoš, J., Kuběna, I., Obrtlík, K., Polák, J., 2015. AFM and SEM-FEG study on fundamental mechanisms leading to fatigue crack initiation. Int. J. Fatigue 76, 11–18. https://doi.org/10.1016/j.ijfatigue.2014.09.019.

Mansfield, C., Cartwright, J., 2001. Fault growth by segment linkage: observations and implications from analogue models. J. Struct. Geol. 23, 745–763.

McFadden, L.D., Eppes, M.C., Gillespie, A.R., Hallet, B., 2005. Physical weathering in arid landscapes due to diurnal variation in the direction of solar heating. Geol. Soc. Am. Bull. 117, 161–173.

Mège, D., Purcell, P., Pochat, S., Guidat, T., 2015. The landscape and landforms of the Ogaden, Southeast Ethiopia. In: Billi, P. (Ed.), Landscapes and Landforms of Ethiopia. Springer, pp. 323–348. https://doi.org/10.1007/978-94-017-8026-1_19.

Menéndez, B., David, C., Nistal, A.M., 2001. Confocal scanning laser microscopy applied to the study of pore and crack networks in rocks. Comput. Geosci. 27, 1101–1109. https://doi.org/10.1016/S0098-3004(00)00151-5.

Moores, J.E., Schuerger, A.C., 2012. UV degradation of accreted organics on Mars: IPD longevity, surface reservoir of organics, and relevance to the detection of methane in the atmosphere. J. Geophys. Res. 117, E08008. https://doi.org/10.1029/2012JE004060.

Moores, J.E., Pelletier, J.D., Smith, P.H., 2008. Crack propagation by differential insolation on desert clast surfaces. Geomorphology 102, 472–481.

Murugesapillai, D., McCauley, M.J., Maher III, L.J., Williams, M.C., 2017. Single-molecule studies of high-mobility group B architectural DNA bending proteins. Biophys. Rev. 9, 17–40.

Nečas, D., Klapetek, P., 2012. Gwyddion: an open-source software for SPM data analysis. Cent. Eur. J. Phys. 10, 181–188.

Nye, H.-Y., McIntyre, N.S., 2007. Unstable amplitude and noisy image induced by tip contamination in dynamic force mode atomic force microscopy. Rev. Sci. Instrum. 78, 023701.

Onishi, C.T., Shimizu, I., 2005. Microcrack networks in granite affected by a fault zone: visualization by confocal laser scanning microscopy. J. Struct. Geol. 27, 2268–2280.

Park, B.C., Song, W., Kim, D.H., Lee, J.-Y., Hong, J., Kim, J.S., 2014. Cross-sectional atomic force microscope in scanning electron microscope. J. Vac. Sci. Technol. B 32, 06FC04. https://doi.org/10.1116/1.4901565.

Pike, W.T., Staufer, U., Hecht, M.H., Goetz, W., Parrat, D., Sykulska-Lawrence, H., Vijendran, S., Madsen, M.B., 2011. Quantification of the dry history of the Martian soil inferred from in situ microscopy. Geophys. Res. Lett. 38, L24201. https://doi.org/10.1029/2011GL049896.

Reches, Z., Lockner, D.A., 2010. Fault weakening and earthquake instability by powder lubrication. Nature 467, 452–456.

Rowe, K.J., Rutter, E.H., 1990. Paleostress estimation using calcite twinning: experimental calibration and application to nature. J. Struct. Geol. 12, 1–17.

Russell, P., Batchelor, D., Thornton, J., 2001. SEM and AFM: complementary techniques for surface investigations. Microsc. Anal. 7, 9–12.

Seydoux-Guillaume, A.M., Montel, J.M., Wirth, R., Moine, B., 2009. Radiation damages in diopside and calcite crystals from uranothorianite inclusions. Chem. Geol. 261, 318–332.

Schultz, R.A., 1995. Limits on strength and deformation properties of jointed basaltic rock masses. Rock Mech. Rock Eng. 28, 1–15.

Schultz, R.A., Klimczak, C., Fossen, H., Olson, J.E., Exner, U., Reeves, D.M., Soliva, R., 2013. Statistical tests of scaling relationships foe geologic structures. J. Struct. Geol. 48, 85–94.

Seydoux-Guillaume, A.-M., Montel, J.M., Bing, B., Bosse, V., de Parseval, P., Paquette, J.-L., Janots, E., Wirth, R., 2012. Low-temperature alteration of monazite: fluid-mediated coupled dissolution–precipitation, irradiation damage, and disturbance of the U–Pb and Th–Pb chronometers. Chem. Geol. 330–331, 140–158.

Siman-Tov, S., Aharonov, E., Sagy, A., Emmanuel, S., 2013. Nanograins from carbonate fault mirrors. Geology 41, 703–706.

Smith, P.H., Tamppari, L.K., Arvidson, R.E., Bass, D., Blaney, D., Boynton, W.V., Carswell, A., Catling, D.C., Clark, B.C., Duck, T., DeJong, E., Fisher, D., Goetz, W., Gunnlaugsson, H.P., Hecht, M.H., Hipkin, V., Hoffman, J., Hviid, S.F., Keller, H.U., Kounaves, S.P., Lange, C.F., Lemmon, M.T., Madsen, M.B., Markiewicz, W.J., Marshall, J., McKay, C.P., Mellon, M.T., Ming, D.W., Morris, R.V., Pike, W.T., Renno, N., Staufer, U., Stoker, C., Taylor, P., Whiteway, J.A., Zent, A.P., 2009. H_2O at the Phoenix landing site. Science 325, 58–60.

Sneddon, I.N., 1946. The distribution of stress in the neighbourhood of a crack in an elastic solid. Proc. R. Soc. A 187, 229–260.

Soyan, D., Gloaguen, R., 2011. Nucleation and Growth of Geological Faults: Nonlinear Processes in Geophysics, vol. 18. pp. 529–536.

Stabile, T.A., Satriano, C., Orefice, A., Festa, G., Zollo, A., 2012. Anatomy of micro-earthquake sequence on an active normal fault. Sci. Rep. 2, 410. https://doi.org/10.1038/srep00410.

Steele, A., Goddard, D.T., Stapleton, D., Toporsli, J.K., Peters, V., Bassinger, V., Sharpless, G., Wynn-Williams, D.D., McKay, D.S., 2000. Investigations into an unknown organism on the martian meteorite allan hills 84001. Meteoritics Planet Sci. 35, 237–241.

Tahmasebi, P., Javadpour, F., Sahimi, M., 2015. Multiscale and multiresolution modeling of shales and their flow and morphological properties. Sci. Rep. 5, 16373. https://doi.org/10.1038/srep16373.

Thomas, E.L.H., Mandal, S., Brusseau, E., Williams, O., 2014. Silica based polishing of {100} and {111} single crystal diamond. Sci. Technol. Adv. Mater. 15, 035013. https://doi.org/10.1088/1468-6996/15/3/035013.

Verati, C., Jourdan, F., 2013. Modelling effect of sericitization of plagioclase on the 40K/40Ar and 40Ar/39Ar chronometers: implication for dating basaltic rocks and mineral deposits. In: In: Jourdan, F., Mark, D.F., Verati, C. (Eds.), Advances in $^{40}Ar/^{39}Ar$ Dating: from Archaeology to Planetary Sciences: London, vol. 378. Geological Society, Special Publication, pp. 155–174.

Voigtländer, A., Leigh, K., Krautblatter, M., 2018. Subcritical crack growth and progressive failure in Carrara marble under wet and dry conditions. J. Geophys. Res. 123. https://doi.org/10.1029/2017JB014956.

Walsh, J.J., Watterson, J., 1989. Displacement gradients on fault surfaces. J. Struct. Geol. 11, 307–316.

Westergaard, H.M., 1939. Bearing pressures and cracks. J. Appl. Mech. 6, A49–A53.

Willemse, E.J.M., 1997. Segmented normal faults: correspondence between three- dimensional mechanical models and field data. J. Geophys. Res. 102 6758–692.

Zagonel, L.F., Mazzucco, S., Tencé, M., March, K., Bernard, R., Laslier, B., Jacopin, G., Tchernycheva, M., Rigutti, L., Julien, F.H., Songmunang, R., Kociak, M., 2011. Nanometer scale spectral imaging of quantum emitters in nanowires and its correlation to their atomically resolved structure. Nano Lett. 11, 568–573.

Zhou, S.W., Xia, C.C., Hu, Y.S., Zhou, Y., Zhang, Y.P., 2015. Damage modeling of basaltic rock subjected to cyclic temperature and uniaxial stress. Int. J. Rock Mech. Min. Sci. 77, 163–173.